



Comparison of nonlinear filtering techniques for photonic systems with blackbody radiation

ISAAC SPOTTS,¹ C. HARRISON BRODIE,¹ S. ANDREW GADSDEN,^{1,3} MOHAMMAD AL-SHABI,² AND CHRISTOPHER M. COLLIER^{1,*}

¹*School of Engineering, University of Guelph, Guelph, Ontario N1G 2W1, Canada*

²*Department of Mechanical and Nuclear Engineering, University of Sharjah, Sharjah, United Arab Emirates*

³*e-mail: gadsden@uoguelph.ca*

**Corresponding author: iccollier@uoguelph.ca*

Received 23 July 2020; revised 16 September 2020; accepted 20 September 2020; posted 21 September 2020 (Doc. ID 403484); published 13 October 2020

This work explores a theoretical solution for noise reduction in photonic systems using blackbody radiators. Traditionally, signal noise can be reduced by increasing the integration time during signal acquisition. However, increasing the integration time during signal acquisition will reduce the acquisition speed of the signal. By developing and applying a filter using a model based on the theoretical equations for blackbody radiation, the noise of the signal can be reduced without increasing integration time. In this work, three filters, extended Kalman filter, unscented Kalman filter (UKF), and extended sliding innovation filter (ESIF), are compared for blackbody photonic systems. The filters are tested on a simulated signal from five scenarios, each simulating different experimental conditions. In particular, the nonlinear filters, UKF and ESIF, showed a significant reduction of noise from the simulated signal in each scenario. The results show great promise for photonic systems using blackbody radiators that require post-process for noise reduction. © 2020 Optical Society of America

<https://doi.org/10.1364/AO.403484>

1. INTRODUCTION

Estimation theory is the branch of science that is used to estimate the true value of a parameter in a system that contains a random element [1]. Estimation theory is commonly used to improve the interpretation of sensor signals [1]. This is advantageous to sensors that have a component of unstructured noise [2]. The behavior of unstructured noise can be modeled as a Gaussian distribution with a mean of zero [2]. With estimation theory, a filter can be developed to reduce the noise generated by photonic emitters with unstructured noise.

For such a filter to be developed, the behavior represented by a model of the measured system is important for the prediction of the true value of a system. The well-known Kalman filter (KF) generates an optimal gain for a linear system to predict the true values of a system, given the previous measurements and a valid model [3]. Using the Kalman filter for these predictions can help determine the actual value of the system using the system characteristics [3]. This is valuable for designs that have poor photonic sensor performance (i.e., high noise) and a known system model that is linear [4]. The Kalman filter can also be applied to nonlinear systems by applying a non-ideal solution to the model through a non-ideal filter.

Two commonly used non-ideal filters are the extended Kalman filter (EKF) [5] and the unscented Kalman filter (UKF)

[6,7]. Integration of the linear and nonlinear recursive-filtering-based estimation techniques has become ubiquitous in modern applications such as robotics [8], position tracking [6], and state estimation of control systems [9]. In robotics, these filtering methods have been applied to assist multiple simulated robots exploring an unknown environment using backtracking techniques [8]. In air traffic control applications, these filtering methods have been applied to motion tracking to determine actual positions of airplanes during their flight path in the presence of noise and clutter [6]. The linear and nonlinear filtering methods tested in position tracking for a simulated air traffic control problem proved successful in providing a more accurate position tracking than the sensor measurements [6]. To increase performance of the state estimation in a proportional integral derivative (PID) controller, an adaptive controller of a simulated electromechanical system was produced using an interacting multiple model (IMM) controller [9].

Although KF-based methods have been used in the above-described application, KF-based methods are derived based on a number of strict assumptions (e.g., the system and measurement noise are white noise, and the system and measurement models are known) [10]. If these assumptions are violated, the KF results may deviate from the true state values. Recently, a new filter, referred to as the sliding innovation filter (SIF) and

presented in Ref. [11], offered a solution to the KF robustness issues. The SIF is based on sliding mode theory, which utilizes a switching gain to keep the estimates close to the true state trajectory. Although a sub-optimal solution, the SIF provides robustness to modeling uncertainties and disturbances, and is demonstrated to be more robust than the KF [11].

Linear and nonlinear filtering methods such as the KF, EKF, and UKF have been introduced in less common applications like photonic systems. Photonic systems are highly predictable, and lend themselves favorably to being represented accurately mathematically [12]. Given that these photonic systems are well known, an application of a filtering method would be beneficial to increasing system performance [13]. Applying recursive estimation techniques to photonic systems is of great interest through signal-to-noise (SNR) ratio improvement and applications in imaging, motion tracking, and spectroscopy. Such filtering can have a great impact on photonic systems research.

Photonic systems research has recently started leveraging the KF to improve system signal-to-noise ratio (SNR) performance. Kalman filtering techniques have been applied to light-emitting diode communications using EKF-based alignment [5], minimization of time delay in position tracking using light-emitting diode infrastructure [12], and diffuse optical tomography parameter estimation [13]. Furthermore, the KF has been used in adaptive optics to improve temporal error introduced through integral controllers [14], and compensation for atmospheric disturbances when imaging astrophysical features [15]. Additionally, fiber-optic systems involving the transmission of light through a fibrous media [16] benefit from the use of KF methods. Complications arise from transporting light over long distances in a media in fiber-optics, such as phase delay and polarization and amplitude decay [17]. Kalman filtering has been applied to fiber-optic technologies for denoising gyroscope signals [1,18] and polarization tracking in communications [19,20].

Kalman filtering has started to see applications in photonic systems, in particular through imaging systems. Imaging describes the branch of optics that deals with the acquisition of electromagnetic data from a sensor and transcribing that information into a visual representation [21]. Image processing occurs after the electromagnetic data is collected, and further data refinement can be used to enhance the image quality [21]. Kalman filtering has been used to improve image processing in state estimation during the image formation of a dynamic object [21,22], the sub-pixel detection of spectral signatures [23], and image stabilization [24]. Biomedical imaging is the image acquisition and visualization of biological matter. Biomedical imaging is a more complicated sub-field of imaging, as the electromagnetic radiation used for acquisition must cause minimal harm to the individual being or biological specimen being examined. Most biomedical imaging techniques make use of electromagnetic radiation, nuclear radiation, and/or ultrasonic air pressure waves. In electromagnetic biomedical imaging, Kalman filtering has been used in surgical guidance [25] and magnetic resonance imaging [26].

Photonic systems and Kalman filtering also connect through motion tracking, which makes use of photonic systems for the position recording of a dynamic object. Electromagnetic waves can be considered the fastest mechanism to record the

position of an object due to the mechanism being constrained by the speed of light. Kalman filtering in motion tracking is used for motion tracking in radar imaging [27], infrared sensor parameter estimation [28], and cross-spectral sensor modeling [29].

Furthermore, Kalman filtering is also used in photonic devices in the field of spectroscopy. Spectroscopy applications such as Fourier transform infrared (FTIR) spectroscopy [30], nuclear spectroscopy [31], and materials optical property estimation [32] have been able to leverage the Kalman filtering technique. Spectroscopy is well established in literature and has become a major part of photonic research as manifested by the use of photonic instrumentation systems. Photonic instrumentation systems measure light intensity using a photosensitive device, like a photodiode or digital image sensor [33,34].

A particularly interesting avenue of research, for its generalized appeal across many applications, is applying Kalman filtering for photonic systems involving the emission and detection of blackbody radiation. However, there is a gap in the literature on applying Kalman filtering directly to the wavelength dimension of a photonic system for improved SNR of photonic systems involving blackbody radiators. The motivation of this paper is to address this literature gap.

In this paper, we demonstrate a simulated spectral analysis of blackbody radiators using two popular Kalman filtering techniques and the new sliding innovation filter strategy. A number of different scenarios are considered to provide a detailed comparison of the nonlinear estimation methods. Each scenario was designed to test different experimental conditions to which a spectrometer can be applied. The filters must be able to read temperatures that are different from the temperature that the filter model uses to predict intensity at each wavelength. The goal of this research is to demonstrate that a filter designed with the behavior of a blackbody radiator can reduce the noise of a simulated measured spectrometer reading. A secondary goal of this research is to determine a preferred filter based on the general performance in all scenarios. Identifying a filter that can be used to decrease noise in simulated spectrometer measurements could indicate potential use for noisy (low integration time) spectrometers to improve signal quality.

The paper is organized as follows. Blackbody radiation and photonic systems are described in Section 2, followed by the nonlinear estimation equations summarized in Section 3. Section 4 provides the simulation setup, and Section 5 provides an overview and discussion of the results. The paper is then concluded in Section 6.

2. BLACKBODY RADIATION AND PHOTONIC SYSTEMS

Blackbody radiation is described in detail here, as it is the focus of the work on Kalman filters. The predictable behavior of blackbody radiation is a key element that allows enhanced SNR performance with the application of Kalman filtering techniques.

Blackbody radiation can be over visible light, which is an important wavelength of interest, for its interaction with the human eye. Visible light is comprised of oscillating electromagnetic radiation (i.e., photons) that exist within the human

perceptual range. The wavelength of the electromagnetic radiation, being the distance between one cycle of oscillation, is the determining property that constitutes the perceived color of light. Humans can distinguish visible light having a wavelength between 400 to 800 nm, with wavelengths shorter than (ultraviolet) and longer than (infrared) this range being invisible. This is important when designing light emitters for human vision. These light emitters can rely on the emission of blackbody radiation, e.g., the sun or fluorescent bulbs. Blackbody emitters that output a uniform white spectrum will be more appealing to the human eye than emitters that output an isolated portion of the visible spectrum. Understanding the governing equations that dictate the emission of light for blackbody radiation is important for these visible blackbody emitters.

Atoms having vibrational kinetic energy, dependent on temperature, give off electromagnetic radiation across many wavelengths (i.e., a spectrum). This temperature-dependent emission is known as blackbody radiation. As a blackbody object heats up, the center wavelength of emitted radiation gradually decreases (i.e., increases in frequency). The blackbody is particularly visible when the center wavelength resides above 800 nm—corresponding to a blackbody temperature above 4000 K. The amplitude per wavelength for a given temperature, $A(\lambda, T)$, for blackbody radiation can be described by

$$A(\lambda, T) = \frac{2hc^2}{\lambda^5} \left(\frac{1}{e^{\frac{hc}{\lambda kT}} - 1} \right), \quad (1)$$

where T is temperature of the blackbody radiator, c is the speed of light in a vacuum, h is Planck's constant, k is Boltzmann's constant, and λ is wavelength.

For the development for a filter model, a temperature must be selected for Eq. (1) to be satisfied. The temperature that is selected will be designated as the calibration temperature. To select a calibration temperature of interest for our Kalman filtering comparison, we consider spectrometers that involve blackbody radiation. In one application, being visible blackbody emitters (incandescent bulbs) and associated spectroscopy, high temperatures are used (5000 K to 6000 K) [35]. As such, we select a calibration temperature of 5500 K for all models developed in this work.

3. NONLINEAR ESTIMATION METHODS

This section describes the three nonlinear filtering methods that are used to estimate blackbody radiation in our simulated photonic system.

A. Extended Kalman Filter

The earliest expansion to nonlinear systems on the Kalman filter (KF) is the extended Kalman filter (EKF). Consider nonlinear system and measurement functions f and h described by Eqs. (2) and (3), respectively:

$$x_{k+1} = f(x_k, u_k) + w_k, \quad (2)$$

$$z_{k+1} = h(x_{k+1}) + v_{k+1}, \quad (3)$$

where x_k refers to the state at time k , u_k refers to the system input, w_k refers to the system noise, z_k refers to the measurement, and v_k is the measurement noise. Both the system and measurement noise are considered white noise (zero mean and normally distributed).

The EKF uses the Jacobian matrices (first-order Taylor series approximations) to linearize the nonlinearities. Equations (4) and (5) represent the linearization of the nonlinear system and measurement functions, respectively:

$$F_{k+1} = \left. \frac{\partial f}{\partial x} \right|_{\hat{x}_{k|k}, u_k}, \quad (4)$$

$$H_{k+1} = \left. \frac{\partial h}{\partial x} \right|_{\hat{x}_{k+1|k}}. \quad (5)$$

The goal of any estimator (e.g., EKF, UKF, or SIF) is to retrieve the true state value x_{k+1} , in this application the intensity observed by a spectrometer reading at a given wavelength (λ), using high noise measurements z_{k+1} . These high noise value can be introduced by electrical components and modeled as white noise [36]. As described in [10], the EKF is created as a predictor-corrector strategy. The prediction stage includes predicting the state estimates as per (6), predicting the state error covariance matrix (the amount of error is represented by the amount of error present in the estimation process) as per (7), and calculating the innovation (measurement error) as per (8):

$$\hat{x}_{k+1|k} = f(\hat{x}_{k|k}, u_k), \quad (6)$$

$$P_{k+1|k} = F_{k+1} P_{k|k} F_{k+1}^T + Q_{k+1}, \quad (7)$$

$$\tilde{z}_{k+1|k} = z_{k+1} - h(\hat{x}_{k+1|k}), \quad (8)$$

where Q represents the system noise covariance matrix, and the subscript $k + 1|k$ refers to the *a priori* ("before the fact") information (prediction stage). In the update stage, the EKF gain is calculated as per (9), which updates the state estimates in Eq. (10), as well as the state error covariance matrix in Eq. (11):

$$K_{k+1} = H_{k+1} P_{k+1|k}^T (H_{k+1} P_{k+1|k} H_{k+1}^T + R_{k+1})^{-1}, \quad (9)$$

$$\hat{x}_{k+1|k+1} = \hat{x}_{k+1|k} + K_{k+1} \tilde{z}_{k+1|k}, \quad (10)$$

$$P_{k+1|k+1} = (I - K_{k+1} H_{k+1}) P_{k+1|k} (I - K_{k+1} H_{k+1})^T + K_{k+1} R_{k+1} K_{k+1}^T, \quad (11)$$

where R_k represents the measurement noise covariance matrix and I is an identity matrix of dimensions $n \times n$, where n is the number of states. Note further that $k + 1|k + 1$ refers to the *a posteriori* ("after the fact") information.

The EKF estimation process is represented by Eqs. (4) through (11), and are used for systems and measurements modeled by Eqs. (2) and (3). The process is repeated iteratively (at each time step).

B. Unscented Kalman Filter

The unscented Kalman filter is another type of nonlinear KF-based method. The UKF is considered more accurate than the EKF for highly nonlinear systems, considering no first-order approximations are used [37]. The UKF can be identified as a sigma-point KF which uses the unscented transform to approximate the nonlinearities. It is also formulated as a predictor-corrector strategy, and can be summarized in five steps.

The generation of $2n + 1$ sigma-points (also called sample points) is the first step. These sigma points will be used to approximate an n state system. The initial sigma point and its corresponding weight (used later) are defined respectively as follows:

$$X_{0,k|k} = \hat{x}_{k|k}, \tag{12}$$

$$W_0 = \frac{\kappa}{n + \kappa}, \tag{13}$$

where κ is a design value typically much less than 1. The remaining $2n$ number of sigma points and their corresponding weights are defined respectively as

$$X_{i,k|k} = \hat{x}_{k|k} \pm \left(\sqrt{(n + \kappa) P_{k|k}} \right)_i, \tag{14}$$

$$W_i = \frac{1}{[2(n + \kappa)]}, \tag{15}$$

where i refers to the i^{th} sigma point. Note that the i term in the square root in Eq. (14) refers to the i^{th} row or column of the matrix square root result.

Calculating the predicted state estimates and covariance is the second step. The sigma points are propagated through the nonlinear system model as per Eq. (16), and the weights are used to calculate the predicted state estimates as per Eq. (17):

$$\hat{X}_{i,k+1|k} = f(X_{i,k|k}, u_k), \tag{16}$$

$$\hat{x}_{k+1|k} = \sum_{i=0}^{2n} W_i \hat{X}_{i,k+1|k}. \tag{17}$$

The values of Eqs. (16) and (17) are used to calculate the state error covariance matrix per Eq. (18):

$$P_{k+1|k} = \sum_{i=0}^{2n} W_i (\hat{X}_{i,k+1|k} - \hat{x}_{k+1|k})(\hat{X}_{i,k+1|k} - \hat{x}_{k+1|k})^T + Q_k. \tag{18}$$

The measurement and measurement (innovation) covariance are calculated in the third step. The sigma points are propagated through the nonlinear measurement model as per Eq. (19), and the measurement is predicted as per Eq. (20):

$$\hat{Z}_{i,k+1|k} = h(\hat{X}_{i,k+1|k}, u_k), \tag{19}$$

$$\hat{z}_{k+1|k} = \sum_{i=0}^{2n} W_i \hat{Z}_{i,k+1|k}. \tag{20}$$

The measurement (innovation) covariance is calculated using Eqs. (19) and (20) as follows:

$$P_{zz,k+1|k} = \sum_{i=0}^{2n} W_i (\hat{Z}_{i,k+1|k} - \hat{z}_{k+1|k})(\hat{Z}_{i,k+1|k} - \hat{z}_{k+1|k})^T + R_{k+1}. \tag{21}$$

The calculation of the cross-covariance as per Eq. (22) in conjunction with Eq. (21) to calculate the UKF gain is the fourth step:

$$P_{xz,k+1|k} = \sum_{i=0}^{2n} W_i (\hat{X}_{i,k+1|k} - \hat{x}_{k+1|k})(\hat{Z}_{i,k+1|k} - \hat{z}_{k+1|k})^T, \tag{22}$$

$$K_{k+1} = P_{xz,k+1|k} P_{zz,k+1|k}^{-1}. \tag{23}$$

The calculation of the updated state estimates as per Eq. (24) and the updated state error covariance matrix as per Eq. (25) is the fifth step:

$$\hat{x}_{k+1|k+1} = \hat{x}_{k+1|k} + K_{k+1}(z_{k+1} - \hat{z}_{k+1|k}), \tag{24}$$

$$P_{k+1|k+1} = P_{k+1|k} - K_{k+1} P_{zz,k+1|k} K_{k+1}^T. \tag{25}$$

The UKF process is summarized by Eqs. (12) through (25), and is repeated iteratively. Although the EKF is mathematically less complex than the UKF, the main advantage to the UKF is that it does not require any linearization, which allows for a more accurate estimate.

C. Sliding Innovation Filter and Extended Sliding Innovation Filter

The sliding innovation filter (SIF) and its nonlinear form, referred to as the extended SIF (ESIF), was recently presented in [11]. It is formulated as a predictor-corrector strategy similar to KF-based methods; however, the gain of the ESIF is derived based on sliding mode techniques. The ESIF provides sub-optimal results for linear systems, but is considered to be more robust than the KF. For nonlinear estimation problems, robustness is maintained while providing comparable accuracy.

The ESIF process is nearly identical to the EKF as presented earlier in Eqs. (2) through (11); however, the gain [Eq. (9)] is different. In this case, the ESIF gain is calculated as follows:

$$K_{k+1} = H_{k+1}^+ \overline{\text{sat}}(|\tilde{z}_{k+1|k}|/\delta), \tag{26}$$

where $+$ represents the pseudoinverse, $\overline{\text{sat}}$ represents a diagonal matrix of elements equal to saturated values, $|\tilde{z}_{k+1|k}|$ refers to the absolute measurement error or innovation, and δ refers to a sliding boundary layer width (one width for each measurement).

Figure 1 provides an overview of the SIF estimation concept. An initial estimate is pushed towards the sliding boundary layer. The amount of uncertainties in the estimation process define the

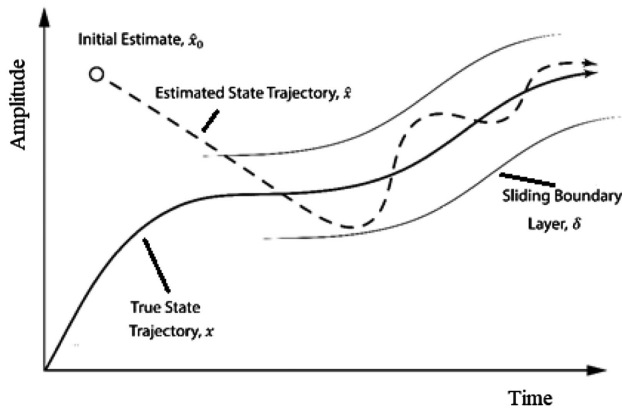


Fig. 1. Illustration of the Sliding Innovation Filter concept [11].

sliding boundary layer. Once inside the sliding boundary layer, the SIF gain forces the estimates to switch about the true state trajectory.

The measurement errors are bounded to the true state trajectory by a switching term, the SIF gain. The function of modeling uncertainty and noise within the estimation process is defined as δ (the sliding boundary layer). Through trial and error, grid search methods, or optimization techniques, the widths can then be tuned to reduce the estimation error.

4. SIMULATION SETUP

All simulations used a wavelength spacing of 10 nm ($d\lambda = 10$ nm). The simulation bounds were $\lambda = 200$ nm to $\lambda = 3400$ nm. The first Kalman filter to be discussed is the EKF. The EKF will use a linearized model of blackbody radiation to predict the system data points. The first state (x) of the filter equation is the intensity given the wavelength as provided by the Steph Boltzmann Eq. (1). The second state (\dot{x}) of this equation is given by the rate of change of the Steph Boltzmann Eq. (1) with respect to wavelength. Using these two states from the previous iteration, an inference can be made about the next intensity value. Randomized noise is added to the system equation represented by w ; this provides a simulated error in spectrometer intensity values. This value is selected to determine how much noise the system will output. The EKF model state equation is as follows:

$$x_{k+1} = \begin{bmatrix} 1 & d\lambda \\ 0 & \alpha - \beta \end{bmatrix} x_k + w_k, \quad (27)$$

where k is the iteration,

$$\alpha = \frac{2h^3 c^3 e^{\frac{hc}{\lambda kT}}}{kT\lambda^7} \left(\frac{1}{e^{\frac{hc}{\lambda kT}} - 1} \right)^2, \quad (28)$$

$$\beta = \left(\frac{10c^2 h}{\left(e^{\frac{hc}{\lambda kT}} - 1 \right) \lambda^6} \right), \quad (29)$$

where $\alpha - \beta$ is the derivative of the blackbody radiation equation with respect to wavelength (\dot{x}), and

$$w = \sim |Q|, \quad (30)$$

where the model system noise covariance Q is

$$Q = \begin{bmatrix} 10^{-2} & 0 \\ 0 & 10^{-2} \end{bmatrix}. \quad (31)$$

The second Kalman filter to be discussed is the UKF. The UKF will leverage the known theoretical model of blackbody radiation to determine the intensity of each wavelength given the noisy measurement. The UKF (and later ESIF) model state equations provided are as follows:

$$x_{k+1} = \begin{bmatrix} 1 & d\lambda(\dot{x}) \\ 0 & \alpha - \beta \end{bmatrix} x_k + w_k. \quad (32)$$

The third filter to be discussed is the ESIF, a sliding mode controller. This filter uses the non-linearized Eq. (32) and the linearized Eq. (27) to generate acceptable bounds in which the next iteration of intensity should be within, given the parameters of the filter. The ESIF uses the tuned δ parameter as a measure of uncertainty. The delta chosen for the ESIF used in these simulations is as follows:

$$\delta = \begin{bmatrix} 4 \times 10^{13} & 0 \\ 0 & 1 \times 10^2 \end{bmatrix}. \quad (33)$$

The calculation on both the sliding parameters δ is completed using an iterative process testing the performance of the filter on a test simulated data set. This iterative process is completed with the calibration temperature (5500 K) simulated data set. The filter is tested with the simulated signal data set and adjusted each iteration to decrease percentage of root mean square error (RMSE) in the post-processed signal. However, this process is only optimized to two significant digits due to overfitting the filter to the calibration data set. If the filter had been to optimal for the calibration data set, then the filter would not optimally perform at other temperatures. Once the sliding parameter, δ , is optimized to the data set, it is used in the filter.

The sliding parameter value, δ , is dependent on the application and can be tuned further if more about the system is prior knowledge. To increase accuracy, it should be decreased. However, doing so will result in a loss of robustness. In this application, temperature change (Scenario 4) and wavelength absorption values (Scenario 5) are simulated, which both require the filter to be robust, for the disturbances to the system to be handled by the filter. Thus, this sliding parameter value, δ , is chosen to accommodate all scenarios.

Each filter is simulated in five different scenarios, with respect to the calibration temperature. The errors in the signals are quantified as the RMSE between the actual signal and the assessed signal. A percent reduction of RMSE can be calculated using the RMSE of the filtered signal and RMSE of the simulated signal.

The state equations are dependent on a calibration temperature. The calibration temperature is a tunable parameter used in the filter to define a central point where the model of the filter will be most similar to the actual model. The calibration temperature in the Kalman filters used is 5500 K. As the actual temperature increases from the calibration temperature, a decrease in filter performance will occur. The model provided tracks the derivative of Planck's law to calculate the next intensity value for a given wavelength. The model does not use the

base Planck's law equation to calculate the exact point because otherwise the model will follow the exact model for the calibration temperature instead of the simulated signal temperature. The measurement equations are as follows:

$$z_{k+1} = \begin{bmatrix} \frac{2bc^2}{\lambda^5} \left(\frac{1}{e^{\frac{hc}{\lambda kT}} - 1} \right) & 0 \\ 0 & \alpha - \beta \end{bmatrix} z_k + v_k, \quad (34)$$

where v is measurement noise expressed by a random value equal to

$$v \sim \left| R \times \frac{10x_{690\text{nm}}}{7} \right|, \quad (35)$$

where $x_{690\text{nm}}$ is the intensity of the blackbody radiation at a wavelength of 690 nm at the scenario temperature. A value of the system is chosen to scale the noise as intensity of the system changes, given the model temperature. Where the measurement noise covariance R is

$$R = \begin{bmatrix} 25 & 0 \\ 0 & 25 \end{bmatrix}, \quad (36)$$

the measurement covariance is a system noise value obtained for the filters to be tested on. The matrix in Eq. (36) could increase or decrease based on the noise in the measurement device, in this application, a spectrometer.

5. RESULTS AND DISCUSSION

Three filters (EKF, UKF, and ESIF) are implemented to determine their effectiveness in reducing the percent RMSE of a simulated signal from five scenarios. A predicted temperature can also be extracted from the spectra provided by the filters. The predicted temperature is identified by a curve-fitting technique that integrates the RMSE between the Stephen Boltzmann Eq. (1) and the filter result to best identify the closest temperature spectrum. Each scenario demonstrates an important application of a spectrometer photonic system reading blackbody radiation. Scenario one is a simulated blackbody radiation spectral reading of a temperature 500 K below the

calibration temperature (5000 K). Scenario two is a simulated blackbody radiation spectral reading of a temperature at the calibration temperature (5500 K). Scenario three is a simulated blackbody spectral reading of a temperature 500 K above the calibration temperature (6000 K). Scenario four is a simulation of a blackbody radiation scan where the spectrometer has been disturbed during the scan. Scenario four was conducted at two temperatures, calibration temperature (5500 K) and the above-calibration temperature (6000 K). Scenario five is a simulation of a blackbody radiation scan at calibration temperature (5500 K), where the spectrometer is reading absorption lines of contaminants in a hypothetical medium. In Table 1, the performance of each filter for every scenario has been quantified in percent RMSE reduction. The percent RMSE reduction gives insight into the ability of the filter to change the simulated signal to be more representative of the true signal.

Figure 2 displays the results from scenario one, being a simulated blackbody radiation spectral reading of a temperature 500 K below the calibration temperature (5000 K). The below-calibration temperature is 5000 K (i.e., 500 K below the calibration temperature). The measurements from this scenario that a spectrometer would provide are seen in Fig. 2(a). The performance of each filter in Figs. 2(b) and 2(c) implies that the EKF and ESIF have a higher percent RMSE reduction when the temperature is lower than the calibration temperature. The nonlinearities that the filter must track are reduced, thus giving an advantage to the EKF. The EKF has a higher RMSE reduction than the UKF when tracking model temperatures below the calibration temperature (78.4% and 39.1% RMSE reduction, respectively). The ESIF performs best in terms of percent RMSE reduction when the temperature of the model is below the calibration temperature (79.5% RMSE reduction). The EKF and the ESIF have the best temperature prediction of 4980 and 5020 K, respectively ($\Delta T = 20$ K). The UKF performs the worst of the three filters when predicting temperature lower than the calibration temperature, with a prediction of 4970 K ($\Delta T = 30$ K).

Figure 3 displays the results from scenario two, being a simulated blackbody radiation spectral reading of the calibration temperature (5500 K). The calibration temperature of the

Table 1. Tabulated Predicted Temperature and Percent RMSE Reduction from Each Filter (EKF, UKF, and ESIF) at all Simulated Scenarios (below calibration temperature, calibration temperature, above calibration temperature, temperature change mid-scan, and absorption lines)

Scenario	EKF		UKF		ESIF				
	Predicted T Value(s) (K)	RMSE Reduction (%)	Predicted T Value(s) (K)	RMSE Reduction (%)	Predicted T Value(s) (K)	RMSE Reduction (%)			
1: Below calibration temperature T = 5000 K	4980	78.4	4970	39.1	5020	79.5			
2: Calibration temperature T = 5500 K	5450	55.5	5530	68.0	5530	74.2			
3: Above calibration temperature T = 6000 K	5890	-1.0	6040	43.3	6020	62.7			
4: Change in temperature, mid-scan T = 5500 to 6000 K	5450	5450	-6.17	5500	6010	55.0	5500	6000	55.4
5: Absorption lines T = 5500 K	N/A	31.0	N/A	44.4	N/A	44.8			

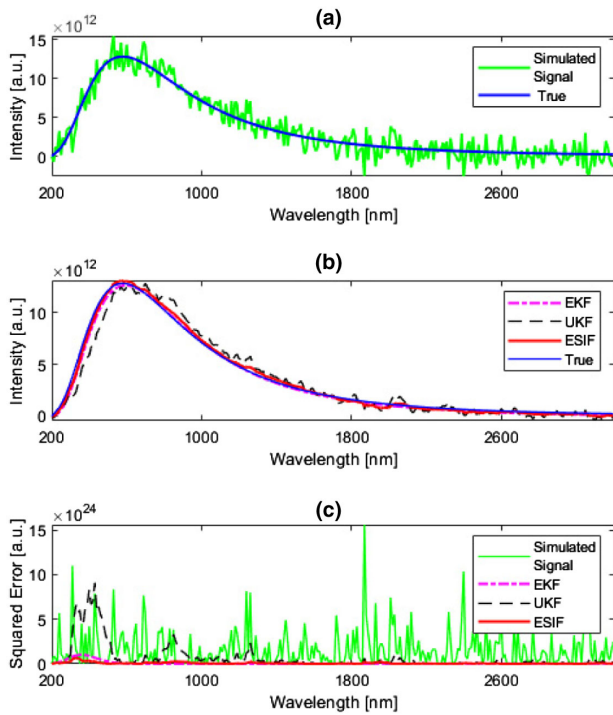


Fig. 2. Graphical display of the results from scenario one, the simulation of blackbody radiation at a temperature 500 K below the calibration temperature. (a) displays the theoretical values of a blackbody radiation spectrum at 5000 K, with the simulated measured data overlaid on the theoretical values. The graph depicted in (b) displays the intensity values of a blackbody radiation spectrum at 5000 K with each filter (EKF, UKF, and ESIF) output using the measured data. (c) displays the squared error of the simulated measurement and each filter at each wavelength data point.

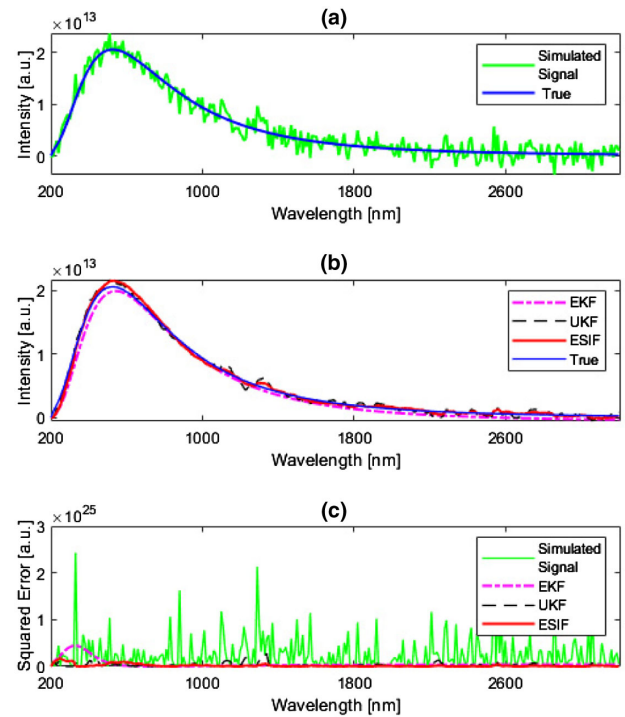


Fig. 3. Graphical display of the results from scenario two, the simulation of blackbody radiation at the temperature calibration temperature. The graph depicted in (a) displays the theoretical values of a blackbody radiation spectrum at 5500 K with the simulated measured data overlaid of the theoretical values. The graph depicted in (b) displays the intensity values of a blackbody radiation spectrum at 5500 K with each filter (EKF, UKF, and ESIF) output using the measured data. The graph depicted in (c) displays the squared error of the simulated measurement and each filter at each wavelength data point.

model is tuned to 5500 K. The measurements from this scenario that a spectrometer would provide are seen in Fig. 3(a). Each filter does not perfectly predict the calibration temperature because each filter cannot only rely on the system model. This allows the filters to predict the blackbody radiation spectrum of temperatures that deviate from the calibration temperature. All filters produce a signal that improves the signal with a percent RMSE reduction of 55.5, 68.0, and 74.2 for the EKF, UKF, and ESIF, respectively. These results are summarized in Table 1. Figure 3(c) shows that each filter produces the largest error between $\lambda = 200$ nm and $\lambda = 300$ nm. The UKF and the ESIF have the best temperature prediction of 5530 and 5530 K, respectively ($\Delta T = 30$ K). The EKF performs the worst of the three filters when predicting the temperature, the calibration temperature, with a prediction of 5450 K ($\Delta T = 50$ K).

Figure 4 displays the results from scenario three, being a simulated blackbody radiation spectral reading of a temperature 500 K above the calibration temperature (6000 K). The above-calibration temperature simulated is 6000 K (i.e., 500 K above the calibration temperature) and displayed in Fig. 4(a). The performance of the EKF shown in Figs. 4(b) and 4(c) demonstrates that temperatures above the calibration temperature cause the filter to decrease the quality of the signal in terms of percent RMSE reduction (-1.0). The nonlinearity of the system increases as the calibration temperature is increased above

the calibration temperature. This causes the UKF and ESIF to perform far better in percent RMSE reduction (53.4 and 76.3, respectively) than the EKF. Figure 4(c) demonstrates that the intensity is tracked relatively well, but begins to fail at approximately the same wavelengths as scenario two (i.e., $\lambda = 200$ nm and $\lambda = 300$ nm). Figure 4(b) also demonstrates the ability of the filter to still reduce the jagged characteristic of the noise in the system. The ESIF has the best temperature prediction of 6020 K ($\Delta T = 20$ K). The UKF is the second-best predictor of the three filters at the above-calibration temperature with a predicted temperature of 6040 K ($\Delta T = 40$ K). The EKF performs the worst of the three filters when predicting the temperature, the calibration temperature, with a prediction of 5890 K ($\Delta T = 110$ K).

Figure 5 displays the results from scenario four, being a simulated blackbody radiation spectral reading of a system temperature change of 500 K at $\lambda = 500$ nm. Theoretically, if a spectral camera requires time to scan through the entire spectrum available for measurement, the temperature could change during the scan. A temperature shift can occur during a scan if there is movement applied to the spectrometer causing the device to image a hotter surface. The measurements from this scenario that a spectrometer would provide are seen in Fig. 5(a). To exaggerate the effect of a temperature shift, the temperature that the model uses increases by 500 K (from 5500 to 6000 K at

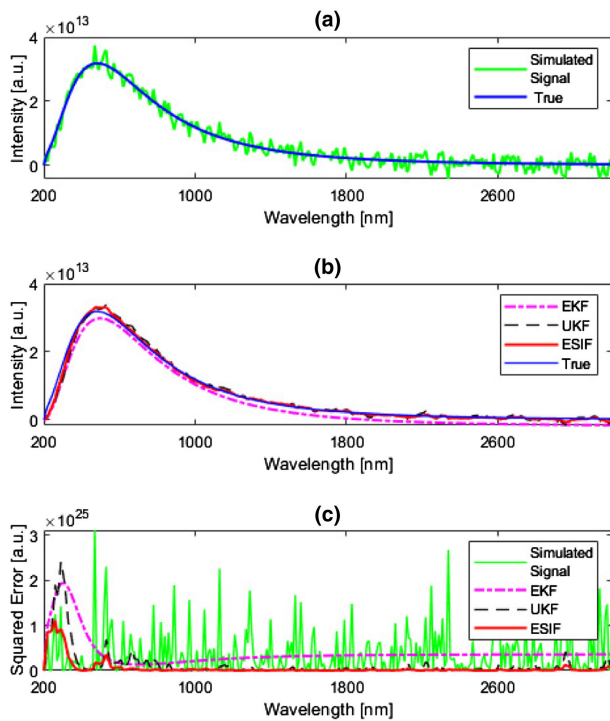


Fig. 4. Graphical display of the results from scenario three, the simulation of blackbody radiation at a temperature 500 K above the calibration temperature. The graph depicted in (a) displays the theoretical values of a blackbody radiation spectrum at 6000 K with the simulated measured data overlaid on the theoretical values. The graph depicted in (b) displays the intensity values of a blackbody radiation spectrum at 6000 K with each filter (EKF, UKF, and ESIF) output using the measured data. The graph depicted in (c) displays the squared error of the simulated measurement and each filter at each wavelength data point.

$\lambda = 690$ nm). The filters are then evaluated to determine if the intensity can still be tracked. In Fig. 5(c), the filters can track the true simulated signal, until the disturbance shift occurs. Once the disturbance shift occurs, there is a small wavelength delay before the filters can correct and acceptable tracking returns. Figures 5(b) and 5(c) show that EKF cannot track the temperature change at all. With the temperature shift, the EKF decreases the quality of the signal by a percent RMSE reduction of -6.2 . Figures 5(b) and 5(c) show that the UKF cannot initially track the temperature shift but begins to adjust the model to fit with the temperature shift. With the temperature shift, the UKF improves the signal of the simulated signal with an RSME percent reduction of 55.0 . The ESIF performs similar to the UKF, but still reduces the percent RMSE slightly more (55.4). In scenario four, two temperatures must be predicted, before and after the temperature change. The RMSE curve fitting was applied to all three filters at before and after $\lambda = 500$ nm. The ESIF performed the best at predicting the before and after temperature change, with a prediction of 5500 and 6000 K, respectively ($\Delta T = 0$ K, $\Delta T = 0$ K). The UKF is the second-best predictor of the temperature change with predictions of 5500 K before and 6010 K after the temperature change ($\Delta T = 0$ K, $\Delta T = 10$ K). The EKF was unable to predict the temperature

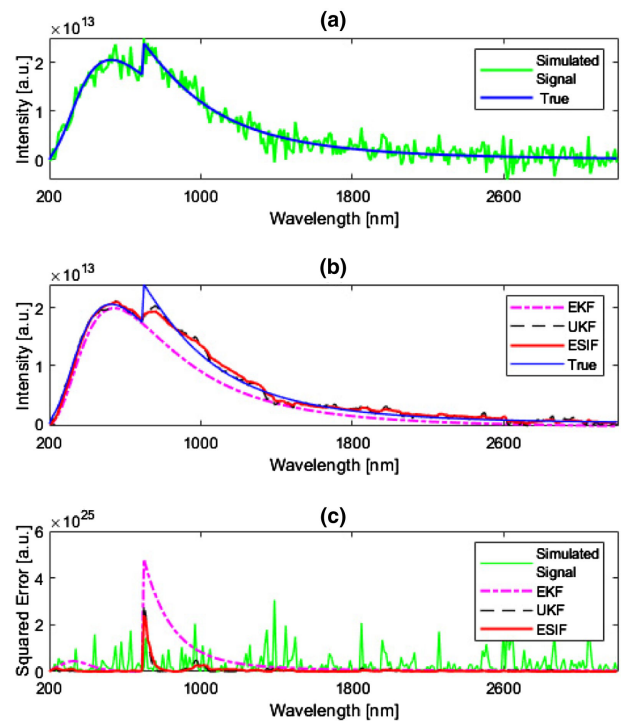


Fig. 5. Graphical display of the results from scenario four, the simulation of blackbody radiation with a temperature change in the blackbody radiator from 5500 to 6000 K. The graph depicted in (a) displays the theoretical values of a blackbody radiation spectrum with temperature change, with the simulated measured data overlaid on the theoretical values. The graph depicted in (b) displays the intensity values of a blackbody radiation spectrum with a temperature change for each filter (EKF, UKF, and ESIF) output using the measured data. The graph depicted in (c) displays the squared error of the simulated measurement and each filter at each wavelength data point.

change with an accurate before-change prediction, but the prediction did not deviate once the temperature change occurred. The before-temperature-change prediction was 5450 K, and the after-temperature-change prediction was 5450 K ($\Delta T = 50$ K, $\Delta T = 550$ K).

Figure 6 displays the results from scenario five, being a simulated blackbody radiation spectral reading of the calibration temperature, with contaminants in a hypothetical medium that have high absorption coefficients at specified wavelengths ($\lambda = 300$ nm, $\lambda = 400$ nm, $\lambda = 510$ nm). Thus far, the filters were chosen to track the nonlinear generation of the blackbody radiation spectra synonymous with spectral measurements of hot objects. In practical settings, emission spectra are often embedded with notable absorption lines. Absorption lines correspond to vibrational modes of the molecules and substances that absorb such wavelength and impede its transmission. For example, incandescent emitters can contain contaminants which could absorb different wavelengths. With this in mind, we have simulated the blackbody radiation with three unique absorption lines, as seen in Fig. 6. The measurement of such a spectrum with absorption lines is seen on Fig. 6(a). The EKF, like scenario four, ignores the nonlinearities observed in the simulated signal. The EKF performs the worst when tracking the spectra with absorption line, providing a percent RMSE

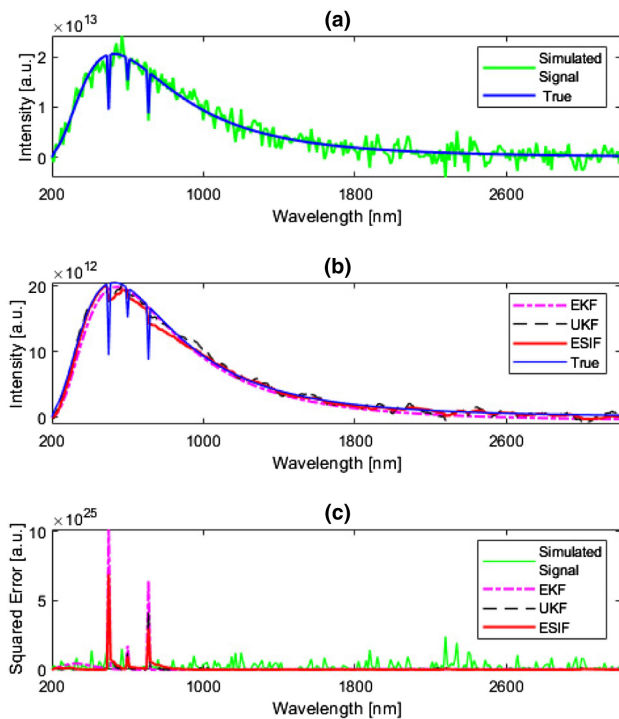


Fig. 6. Graphical display of the results from scenario five, the simulation of blackbody radiation with contaminants in a hypothetical medium of radiation travel, resulting in absorption lines. The graph depicted in (a) displays the theoretical values of a blackbody radiation spectrum with absorption lines at 5500 K with the simulated measured data overlaid on the theoretical values. The graph depicted in (b) displays the intensity values of a blackbody radiation spectrum with absorption lines at 5500 K with each filter (EKF, UKF, and ESIF) output using the measured data. The graph depicted in (c) displays the squared error of the simulated measurement and each filter at each wavelength data point.

reduction of 31.0. The UKF can approximate the sharp transitions at a large decrease in intensity that the system outputs. The ESIF can also track the absorption lines in Fig. 6(c) like the UKF, providing less loss in intensity from each peak than the UKF. Overall, the ESIF performs better when tracking the absorption lines, with a percent RMSE reduction of 44.8 in comparison to the UKF percent RMSE reduction of 44.4. The prediction of the absorption wavelength with the ESIF was on average the most accurate out of the three filters with the absorption wavelengths occurring at $\lambda = 300$ nm, $\lambda = 400$ nm, and $\lambda = 510$ nm, with absorption values of 24.3%, 32.2%, and 33.4%, respectively, of the simulated absorption value. The UKF could also predict the absorption values at the absorption wavelengths $\lambda = 300$ nm, $\lambda = 400$ nm, and $\lambda = 510$ nm, with predictions of 25.8%, 24.0%, and 20.9%, respectively, of the simulated absorption value. The EKF could not predict the absorption wavelength and the data values were unchanged by the absorption lines (0%, 0%, and 0% for $\lambda = 300$ nm, $\lambda = 400$ nm, and $\lambda = 510$ nm, respectively). The absorption wavelength shift is found through comparing local maxima in results. The absorption wavelength shift for the filters that had a percent reduction in amplitude was 0 nm.

6. CONCLUSION

The Kalman filter has been explored for application to spectroscopy systems with blackbody radiators. Leveraging the blackbody equation, a filter was explored to predict the intensity of a spectrum at each wavelength, with the equation at a calibration temperature as a framework.

The EKF is the worst-performing filter, due to the inability of the EKF to track nonlinearities. The use of the EKF on noise reduction is not recommended because it can worsen the quality of signals above the tuned calibration temperature. Additionally, the EKF did not track disturbances occurring during scans. The EKF has demonstrated in scenarios three, four, and five that the filter cannot predict the non-linearities with worse RMSE reductions (-1.0% and -6.17% , respectively) and the inability to recognize absorption wavelengths. The UKF could not predict the temperature change in scenario four, with the filter still providing predictions for the temperature 5500 K (filter predicted temperature $T = 5450$ K) instead of the changed temperature 6000 K.

The UKF is an acceptable application of the Kalman filter on reduction of noise for blackbody radiation measurements. The UKF demonstrates the capability to improve the quality of the signal in terms of percent RMSE reduction in every scenario. The UKF has demonstrated in scenarios one, two, and three that the filter can predict the non-linearities from high temperatures with sacrificing little prediction to the lower than calibration temperature reading, providing acceptable RMSE reductions (39.1%, 68.0%, and 43.3%, respectively) and the ability to recognize absorption wavelengths in scenario five. The UKF could also recognize the change in temperature and corrected the prediction to determine the new temperature presented with an acceptable percent RMSE reduction (55.0%) and temperature predictions ($T = 5500$ K, $T = 6010$ K).

The novel extended sliding innovation filter (ESIF) is the best-performing filter for every scenario. The ESIF has demonstrated in scenarios one, two, and three that the filter can predict the theoretical signal given the simulated signal, providing the best RMSE reductions (79.5%, 74.2%, and 62.7%, respectively) and the ability to recognize absorption wavelengths in scenario five. The UKF could also recognize the change in temperature and corrected the prediction to determine the new temperature presented with an acceptable percent RMSE reduction (55.4%) and temperature predictions ($T = 5500$ K, $T = 6000$ K). The application of the ESIF would be advantageous on high-speed, low-integration-time spectrometers that possess blackbody radiation characteristics.

Funding. Natural Sciences and Engineering Research Council of Canada (04022).

Disclosures. The authors declare no conflicts of interest.

REFERENCES

1. R. Peesapati, S. L. Sabat, K. P. Karthik, J. Nayak, and N. Giribabu, "Efficient hybrid Kalman filter for denoising fiber optic gyroscope signal," *Optik* **124**, 4549–4556 (2013).

2. C. Jáuregui Misas, J. M. López-Higuera, and M. López-Amo, "Adaptive filters applied to the interrogation of photonic sensors," *IEEE Sens. J.* **6**, 748–753 (2006).
3. S. Y. Chen, Y. Wang, C. C. Wu, C. Liu, and C. I. Chang, "Real-time causal processing of anomaly detection for hyperspectral imagery," *IEEE Trans. Aerosp. Electron. Syst.* **50**, 1511–1534 (2014).
4. M. A. El Sayed, S. A. Gadsden, and S. R. Habibi, "A sliding mode controller based on the interacting multiple model strategy," in *Fluid Power Motion Control (FPMC)* (2012).
5. P. B. Solanki and X. Tan, "Extended Kalman filter-based 3D active-alignment control for LED communication," in *International Conference on Robotics and Automation* (2018), Vol. **23**, pp. 4881–4888.
6. A. Gadsden, S. Habibi, D. Dunne, and T. Kirubarajan, "Nonlinear estimation techniques applied on target tracking problems," *Trans. ASME J. Dyn. Syst. Meas. Control* **134**, 054501 (2012).
7. M. Haghighipanah, M. Miyasaka, Y. Li, and B. Hannaford, "Unscented Kalman filter and 3D vision to improve cable driven surgical robot joint angle estimation," in *International Conference on Robotics and Automation*, June, 2016, pp. 4135–4142.
8. J. Kim, S. Bonadies, C. D. Eggleton, and S. Andrew Gadsden, "Cooperative robot exploration strategy using an efficient back-tracking method for multiple robots," *J. Mech. Robot.* **10**, 1–7 (2018).
9. S. A. Gadsden, "An adaptive PID controller based on Bayesian theory," in *ASME Dynamic Systems and Control Conference*, Tysons Corner, Virginia, USA, 2017, pp. 1–7.
10. S. A. Gadsden, "Smooth variable structure filtering: theory and applications," Ph.D. Dissertation (McMaster University, 2011).
11. S. Gadsden and M. AlShabi, "The sliding innovation filter," *IEEE Access* **8**, 96129–96138 (2020).
12. M. T. Hossain, M. Z. Chowdhury, A. Islam, and Y. M. Jang, "A novel indoor mobile localization system based on optical camera communication," *Wireless Commun. Mob. Comput.* **2018**, 9353428 (2018).
13. G. R. Baez, J. A. Pomarico, and G. E. Elicabe, "An improved extended Kalman filter for diffuse optical tomography," *Biomed. Phys. Eng. Express* **3**, 015013 (2017).
14. T. Fusco, G. Rousset, J. L. Beuzit, D. Mouillet, and K. Dohlen, "High order adaptive optics requirements and feasibility for high contrast imaging," *Proc. Int. Astron. Union* **1**, 513–518 (2005).
15. P. Piatrou and M. C. Roggemann, "Performance study of Kalman filter controller for multiconjugate adaptive optics," *Appl. Opt.* **46**, 1446–1455 (2007).
16. I. Spotts, D. Ismail, N. Jaffar, and C. M. Collier, "Fibre-optic sensing in digital microfluidic devices," *Sens. Actuators A* **280**, 164–169 (2018).
17. E. H. W. Chan, "Suppression of phase-induced intensity noise in fibre optic delay line signal processors using an optical phase modulation technique," *Opt. Express* **18**, 21573–21584 (2010).
18. K. Zhang, W. Tian, and F. Qian, "A novel adaptive filter mechanism for improving the measurement accuracy of the fiber optic gyroscope in the maneuvering case," *Meas. Sci. Technol.* **18**, 2777–2782 (2007).
19. T. Marshall, B. Szafraniec, and B. Nebendahl, "Kalman filter carrier and polarization-state tracking," *Opt. Lett.* **35**, 2203–2205 (2010).
20. G. Cao, Y. Yang, K. Zhong, X. Zhou, Y. Yao, A. P. Tao Lau, and C. Lu, "Fast polarization-state tracking based on radius-directed linear Kalman filter," in *Optical Fiber Communication Conference*, June, 2015, pp. 19673–19680.
21. M. D. Butala, R. A. Frazin, Y. Chen, and F. Kamalabadi, "Tomographic imaging of dynamic objects with the ensemble Kalman filter," *IEEE Trans. Image Process.* **18**, 1573–1587 (2009).
22. M. Piovoso and P. A. Laplante, "Kalman filter recipes for real-time image processing," *Real-Time Imaging* **9**, 433–439 (2003).
23. C. Brumbley and C. I. Chang, "Unsupervised linear unmixing Kalman filtering approach to signature extraction and estimation for remotely sensed imagery," in *IEEE International Geoscience and Remote Sensing Symposium* (1998), Vol. **3**, pp. 1590–1592.
24. T. H. S. Li and C. C. Chen, "Extended Kalman filter based hand-shake detector for optical image stabilization using a low cost gyroscope," *IEEE Trans. Consum. Electron.* **59**, 113–121 (2013).
25. A. Vaccarella, E. De Momi, A. Enquobahrie, and G. Ferrigno, "Unscented Kalman filter based sensor fusion for robust optical and electromagnetic tracking in surgical navigation," *IEEE Trans. Instrum. Meas.* **62**, 2067–2081 (2013).
26. X. Feng, M. Salerno, C. M. Kramer, and C. H. Meyer, "Kalman filter techniques for accelerated Cartesian dynamic cardiac imaging," *Magn. Reson. Med.* **69**, 1346–1356 (2013).
27. R. F. Cinar, F. Kocadag, and A. Demirkol, "Kalman filter aided target density function for radar imaging," *J. Eng.* **2019**, 5602–5604 (2019).
28. Y. Motai, S. Kumar Jha, and D. Kruse, "Human tracking from a mobile agent: optical flow and Kalman filter arbitration," *Signal Process. Image Commun.* **27**, 83–95 (2012).
29. M. Magnabosco and T. P. Breckon, "Cross-spectral visual simultaneous localization and mapping (SLAM) with sensor handover," *Robot. Auton. Syst.* **61**, 195–208 (2013).
30. D. Wilson and C. Allen, "Experimental validation of an unscented Kalman filter for estimating transient engine exhaust composition with Fourier transform infrared spectroscopy," *Energy Fuels* **32**, 11899–11912 (2018).
31. D. G. Abrecht, J. M. Schwantes, R. K. Kukkadapu, B. S. McDonald, G. C. Eiden, and L. E. Sweet, "Real-time noise reduction for Mössbauer spectroscopy through online implementation of a modified Kalman filter," *Nucl. Instrum. Methods Phys. Res. A* **773**, 66–71 (2015).
32. Y. Shen, S. Lou, and X. Wang, "Estimation method of point spread function based on Kalman filter for accurately evaluating real optical properties of photonic crystal fibers," *Appl. Opt.* **53**, 1838–1845 (2014).
33. J. E. Carey, C. H. Crouch, M. Shen, and E. Mazur, "Visible and near-infrared responsivity of femtosecond-laser microstructured silicon photodiodes," *Opt. Lett.* **30**, 1773–1775 (2005).
34. S. Agwani, J. Miller, S. G. Chamberlain, and W. D. Washkurak, "High resolution tri-linear colour TDI CCD image sensor with programmable responsivity gain," in *International Electron Devices Meeting* (1995), pp. 151–154.
35. M. R. Luo, G. Cui, and M. Georgoula, "Colour difference evaluation for white light sources," *Light. Res. Technol.* **47**, 360–369 (2015).
36. M. Marzano, A. Cultrera, M. Ortolano, and L. Callegaro, "A correlation noise spectrometer for flicker noise measurement in graphene samples," *Meas. Sci. Technol.* **30**, 035102 (2019).
37. E. A. Wan and R. Van Der Merwe, "The unscented Kalman filter for nonlinear estimation," in *IEEE Adaptive Systems for Signal Processing, Communications, and Control Symposium (Cat. No.00EX373)* (2000), pp. 153–158.